Performance Improvement of Polymer

Koster, L. Jan Anton; Mihailetchi, Valentin D.; Lenes, Martijn; Blom, Paul W.M.

Published in:
Organic Photovoltaics: Materials, Device Physics, and Manufacturing Technologies

Publication date:
2008

B
Bulk Heterojunction Solar Cells

Organic Photovoltaics: Materials, Device Physics, and Manufacturing Technologies.
Edited by Christoph Brabec, Vladimir Dyakonov, and Ullrich Scherf

ISBN: 978-3-527-31675-5

10
Performance Improvement of Polymer: Fullerene Solar Cells Due to Balanced Charge Transport

L. Jan Anton Koster, Valentin D. Mihailetchi, Martijn Lenes, and Paul W.M. Blom

10.1
Introduction

An attractive way of producing energy is to harvest it directly from sunlight. The amount of energy that the Earth receives from the Sun is enormous: 1.75×10^{17} W. As the world energy consumption in 2003 amounted to 4.4×10^{20} J, Earth receives enough energy to fulfill the yearly world demand of energy in less than an hour. Not all of that energy reaches the Earth's surface due to absorption and scattering, however, and the photovoltaic conversion solar energy remains an important challenge. State-of-the-art inorganic solar cells have a record power conversion efficiency of close to 39% [1], whereas commercially available solar panels have a significantly lower efficiency of around 15–20%. Another approach to making solar cells is to use organic materials such as conjugated polymers. Solar cells based on thin polymer films are particularly attractive because of their ease of processing, mechanical flexibility, and potential for low cost fabrication of large areas. Additionally, their material properties can be tailored by modifying their chemical makeup, resulting in greater customization than traditional solar cells allow.

The field of organic photovoltaics dates back to 1959 when Kallman and Pope discovered that anthracene can be used to make a solar cell [2]. Their device produced a photovoltage of only 0.2 V and had an extremely low efficiency. Attempts to improve the efficiency of solar cells based on a single organic material (a so-called homojunction) were unsuccessful, mainly because of the low dielectric constant of organic materials (typically, the relative dielectric constant is 2–4). Due to this low dielectric constant, the probability of forming free charge carriers upon light absorption is very low. Instead strongly bound excitons are formed, with a binding energy of around 0.4 eV in the case of poly(*p*-phenylene vinylene) (PPV) [3–5]. Since these excitons are so strongly bound, the electric field in a photovoltaic device, which arises from the work function difference between the electrodes, is too weak to dissociate the excitons. A major advancement was realized by Tang who used two different materials, stacked in layers, to dissociate the excitons [6]. In this so-called heterojunction, an electron donor material (D) and an electron acceptor material (A) are brought together.

Organic Photovoltaics: Materials, Device Physics, and Manufacturing Technologies.
Edited by Christoph Brabec, Vladimir Dyakonov, and Ullrich Scherf

ISBN: 978-3-527-31675-5

By carefully matching these materials, electron transfer from the donor to the acceptor, or hole transfer from the acceptor to the donor, is energetically favored. In 1992, Sariciftci *et al.* demonstrated that ultrafast electron transfer takes place from a conjugated polymer to C_{60}, showing the great potential of fullerenes as acceptor materials [7]. To be dissociated, the excitons must be generated in proximity to the donor/acceptor interface, since the diffusion length is typically 5–7 nm [8–10]. This need limits the part of the active layer that contributes to the photocurrent to a very thin region near the donor/acceptor interface; excitons generated in the remainder of the device are lost. How can the problem of all excitons not reaching the donor/acceptor interface be overcome? In 1995 Yu *et al.* devised a solution [11]: by intimately mixing both components, the interfacial area is greatly increased and the distance that excitons have to travel to reach the interface is reduced. This device structure is called a bulk heterojunction (BHJ) and has been used extensively since its introduction in 1995. An important breakthrough in terms of power conversion efficiency was reached by Shaheen *et al.* who showed that the solvent used has a profound effect on the morphology and performance of BHJ solar cells [12]. By optimizing the device processing, an efficiency of 2.5% was obtained. State-of-the-art polymer/fullerene BHJ solar cells have an efficiency of more than 4% [13]. Although significant progress has been made, the efficiency of converting solar energy into electrical power obtained with plastic solar cells still does not warrant commercialization. To improve the efficiency of plastic solar cells, it is, therefore, crucial to understand what limits their performance.

The main steps in photovoltaic energy conversion by organic solar cells are depicted in Figure 10.1.

As a first step, we consider the simple case of a photoconductor with noninjecting contacts and an uniform electric field distribution. Goodman and Rose derived that, under the assumption of negligible recombination of charge carriers [14], the photocurrent J_{ph} is given by

$$J_{\mathrm{ph}} = qGL, \tag{10.1}$$

with q the electron charge, G the generation rate of charge carriers, and L the thickness of the photoconductor. In this case all photogenerated charge carriers are simply extracted and the current density depends only on the generation rate G. In their derivation, Goodman and Rose took only drift of charge carriers into account and neglected the contribution of diffusion. Sokel and Hughes carried this analysis one step further by including diffusion of carriers, finding [15]

$$J_{\mathrm{ph}} = qGL\left[\frac{\exp(V/V_t)+1}{\exp(V/V_t)-1} - 2\frac{V_{\mathrm{t}}}{V}\right], \tag{10.2}$$

where V is the voltage drop across the active layer and V_{t} the thermal voltage, $V_{\mathrm{t}} = kT/q$, where k is Boltzmann's constant and T is the temperature. For a BHJ device with a voltage V_0 already present from the different work functions of the contacts, the voltage drop amounts to $V_0 - V$. The result by Sokel and Hughes shows two regimes: a linear dependence of J_{ph} on voltage for small biases (regime I), while reducing

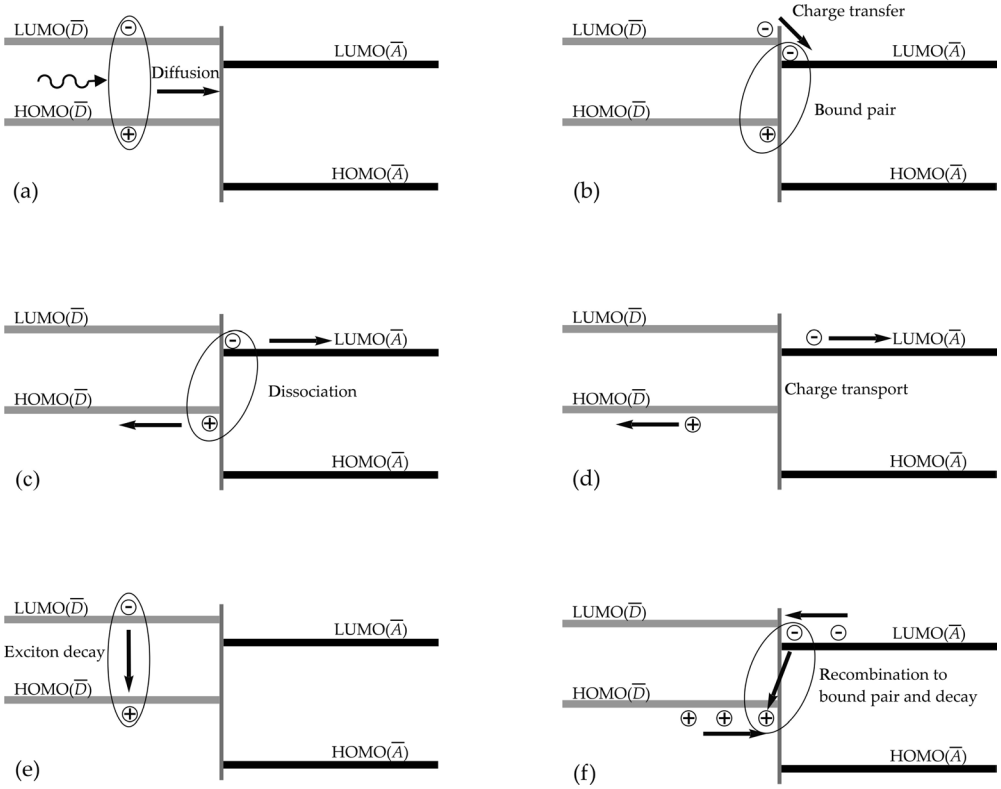

Figure 10.1 Organic photovoltaics in a nutshell: part (a) shows the process of light absorption by the polymer, yielding an exciton that has to diffuse to the donor/acceptor interface. If the exciton reaches this interface, electron transfer to the acceptor phase in energetically favored, as shown in (b), yielding a coulombically bound electron–hole pair. The dissociation of the electron–hole pair, either phonon or field assisted, produces free charge carriers, as depicted in (c). Finally, the free carriers have to be transported through their respective phases to the electrodes to be extracted (d). Exciton decay is one possible loss mechanism, see (e), while geminate recombination of the bound electron–hole pair and bimolecular recombination of free charge carriers (f) are two other possibilities.

to Equation 10.1 at moderately high bias (including short-circuit conditions) (regime II), see Figure 10.2a.

In the case of recombination losses, the extraction of photogenerated carriers is governed by the mean carrier drift length w, which is the mean distance a carrier travels before recombination occurs. When both the electron (w_n) and hole (w_p) drift lengths are larger than the active layer thickness, then the charges will readily flow out without distorting the field in the device, as shown in Figure 10.3a. However, for example, in the case where $w_n \gg w_p$ and $w_p < L$, there will be a net positive space charge near the anode, as shown in Figure 10.3b. For this situation, three regimes exist in the device: near the cathode, the electron density is much larger than the hole density; this is a small region (I). Next to this region, there exists a balance between

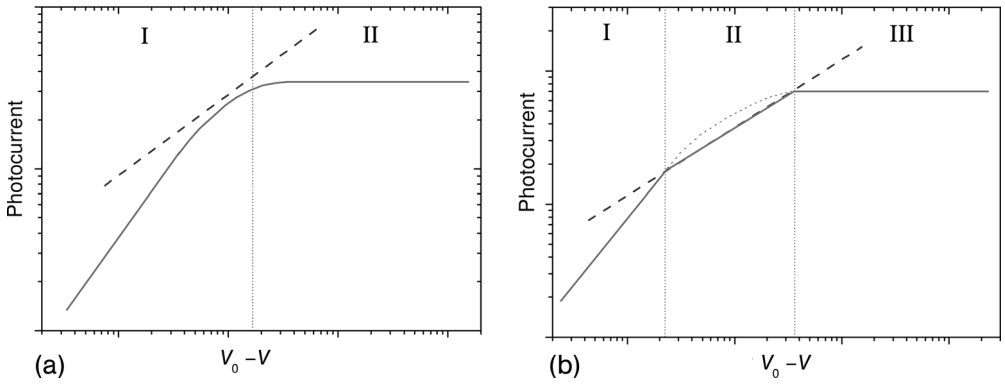

Figure 10.2 Schematic photocurrent versus voltage drop across the active layer for a device without (a) and with (b) space charge limitations. The dashed line represents the space-charge-limited photocurrent, given by Equation 10.2.

electron and hole density, yielding a neutral region (II). Near the anode, the holes dominate the device (III), resulting in a large net space charge and concomitant large voltage drop, as indicated in Figure 10.3b. The large field strength in region III facilitates the extraction of holes, ensuring that the extraction current of holes and electrons is equal. When the photocurrent is space-charge-limited (SCL), the following relation holds [14]:

$$J_{\mathrm{ph}} \leq (qG)^{0.75} \left(\frac{9}{8}\varepsilon_0 \varepsilon_r \mu_h\right)^{0.25} \cdot \sqrt{V}, \tag{10.3}$$

where μ is the mobility of the slowest carrier, holes in this case, and $\varepsilon_0\varepsilon_r$ the dielectric constant. Thus, fully space-charge-limited photocurrents are characterized by a square root dependence on voltage and are proportional to the incident light intensity I as $I^{0.75}$, irrespective of the amount of bimolecular recombination. In that case, as shown in Figure 10.2b, a third regime appears in the J_{ph}–V characteristics,

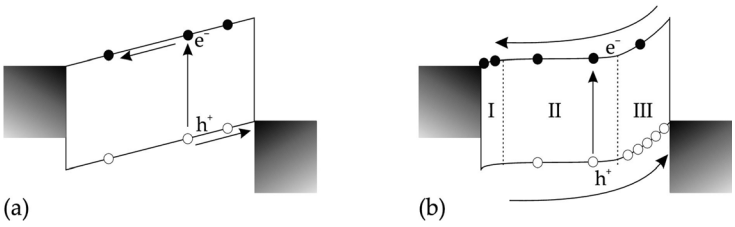

Figure 10.3 (a) Band diagram of a BHJ solar cell with balanced electron and hole mobilities; both types of charge carriers can readily flow out of the device and the field in the device is uniform. (b) Band diagram in the case of hole accumulation and concomitant space-charge-limited behavior. Near to the cathode, a small region dominated by electrons (I) exists next to a large neutral region (II), where electron and hole densities are comparable. Most of the potential drops across the hole accumulation layer (III) to facilitate the extraction of the slow holes.

thereby strongly limiting the fill factor (FF) of the solar cell. The occurrence of space-charge-limited photocurrents in BHJ solar cells based on [6,6]-phenyl C_{61}-butyric acid methyl ester (PCBM) and low mobility PPV derivatives has been demonstrated by Mihailetchi *et al.* [16].

10.2 MDMO-PPV:PCBM-Based Solar Cells

As shown in the previous section, in the case of a large difference in mean-free path for electrons and holes caused by, for example, a large difference in electron and hole mobility, the electric field in the device adjusts itself in such a way that the transport of the slowest carrier is enhanced. This results in a nonuniform field, since the charges of photogenerated electrons and holes do not cancel. Consequently, the slowest charge carrier will dominate the device because the faster carrier can leave the device much more easily. Since the hole mobility of neat poly(2-methoxy-5-(3′,7′-dimethoxy-loctyloxy)-*p*-phenylene vinylene) (MDMO-PPV) was previously reported to be $5 \times 10^{-11}\,m^2\,V^{-1}s^{-1}$ [17], while an electron mobility of $2 \times 10^{-7}\,m^2\,V^{-1}s^{-1}$ was disclosed for [6,6]-phenyl C_{61}-butyric acid methyl ester (PCBM) [18], the charge transport in a heterojunction photovoltaic cell based on these materials is expected to be strongly unbalanced. However, from space-charge-limited conduction, admittance spectroscopy, and transient electroluminescence measurements, a hole mobility of $2 \times 10^{-8}\,m^2\,V^{-1}s^{-1}$ was found for the MDMO-PPV phase in the (1 : 4 wt%) blend at room temperature [19]. Consequently, the charge carrier transport in an MDMO-PPV:PCBM-based solar cell was much more balanced than previously assumed, which is a necessary requirement for the disclosed high fill factors of above 50%. This enhanced mobility is in agreement with the fact that to electrostatically allow the experimentally observed photocurrents, a hole mobility of at least $10^{-8}\,m^2\,V^{-1}s^{-1}$ is required. For lower mobilities the photocurrent is expected to be dominated by a nonuniform electric field and resulting space charge formation, as shown in Figure 10.3b. In that case a square root dependence of the photocurrent on voltage is expected. Figure 10.4 shows the current–voltage characteristics of a 120 nm thick MDMO-PPV:PCBM (1 : 4 by weight) BHJ solar cell. In this graph, the effective photocurrent density J_{ph}, obtained by subtracting the dark current from the current under illumination, is plotted as a function of effective applied voltage $V_0 - V$, where V_0 is the compensation voltage defined by $J_{ph}(V = V_0) = 0$ [20] In this way, $V_0 - V$ reflects the internal electric field in the device. It should be noted that $V_0 = 0.884$ V is very close to the open-circuit voltage (0.848 V). For low effective voltages $V_0 - V$, the photocurrent increases linearly with effective voltage and subsequently tends to saturate. Mihailetchi *et al.* [20] demonstrated that this low-voltage part can be described with an analytical model developed by Sokel and Hughes [15] for zero recombination, as indicated by the dashed line in Figure 10.4. The linear behavior at low effective voltage is the result of a direct competition between diffusion and drift currents. At higher effective voltage all free charge carriers are extracted for zero recombination and the photocurrent saturates to qGL.

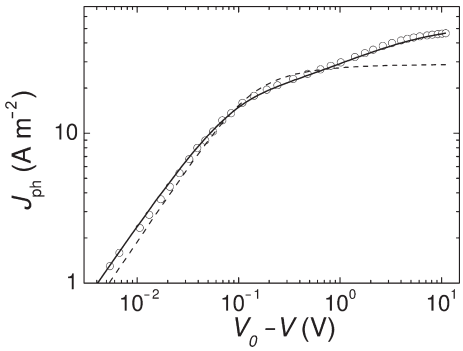

Figure 10.4 Photocurrent density J_{ph} as a function of effective applied voltage ($V_0 - V$). The symbols represent experimental data of MDMO-PPV/PCBM devices at room temperature. The solid line denotes a numerical simulation, while the dashed line represents the result of Sokel and Hughes.

The fact that the experimental photocurrent does not completely saturate at qGL but gradually increases for large effective voltages has been attributed to the field dependence of the generation rate G. The two parameters governing the field- and temperature-dependent generation rate $G(E,T)$ [21], the electron–hole pair distance a, and the decay rate k_f can be determined by equating the high field photocurrents to qGL. The value of a determines the field at which the dissociation efficiency fully saturates and hence a can be determined independent of k_f. By fitting the temperature dependence of the photocurrent at high reverse bias, $a = 1.3$ nm and $k_f = 2.5 \times 10^5\ s^{-1}$ are obtained [20]. Subsequently, these parameters were implemented in a numerical device model to describe the full voltage range [22]. It is evident from Figure 10.4 that the calculated photocurrent fits the experimental data over the entire voltage range. For comparison, in Figure 10.5 the experimental and calculated J_{ph} are also shown in a conventional linear plot focusing on the fourth quadrant.

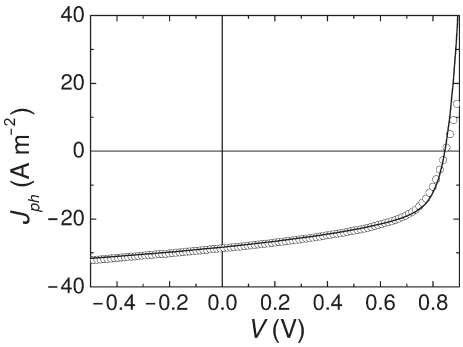

Figure 10.5 The current density under illumination of a MDMO-PPV:PCBM device (symbols) and the numerical result (line).

The excellent agreement between experimental and calculated data now enables one to further analyze the losses in these devices in more detail.

A striking feature of these types of solar cells is that at the optimal device thickness of typically 100 nm, only 60% of the incident light is absorbed [12]. The absorption can be enhanced by increasing the thickness of the active layer. However, in spite of an increased absorption, the overall power conversion efficiency does not improve when the device thickness is increased beyond 100 nm. It is evident that a thickness increase is expected to also give rise to an enhanced charge recombination because of an increase in carrier drift length [23,24]. From a device point of view, the reduced performance with increasing thickness mainly originates from a decrease in the fill factor. As discussed above, for devices with a large difference in electron and hole mobility, a space-charge-limited photocurrent occurs at high intensity due to an unbalanced charge transport, described by Equation 10.3. It should be noted that Equation 10.3 does not depend on device thickness. On the contrary, for nonspace-charge-limited devices, as is the case for standard 100 nm MDMO-PPV:PCBM solar cells, the photocurrent density at short-circuit and reverse bias is closely approximated by $J_{ph} = qG(E,T)L$. Consequently, in this case, increasing the active layer thickness will generally result in a higher photocurrent due to an enhanced absorption. As a result, with increasing active layer thickness at some point the photocurrent will reach the (thickness independent) space charge limit given by Equation 10.3, and a transition will occur from a non-SCL, as shown in Figure 10.2a, to a SCL device as shown in Figure 10.2b. Such a transition will lead to a strong decrease in the fill factor, even when charge recombination does not play a role.

To investigate the effect of space charge formation, the photocurrents of devices with a thin (128 nm) and a thick (368 nm) active layer have been studied in more detail, including their illumination intensity dependence. Figure 10.6 shows the photocurrent density $J_{ph} = J_L - J_D$, where J_L and J_D are the current density under illumination and in dark, respectively, as a function of effective applied voltage $V_0 - V$ for both devices. Also shown is the predicted space charge limit using $\mu_h = 3 \times 10^{-8}\,m^2\,V^{-1}\,s^{-1}$ and $G = 1.9 \times 10^{27}$ and $0.9 \times 10^{27}\,m^{-3}\,s^{-1}$ for both devices. In the case of the 128 nm device, the photocurrent is still below the space charge limit and two regimes can be recognized, as also represented in Figure 10.2a. For voltages close to V_0, the photocurrent scales linearly with effective applied voltage due to a competition between drift and diffusion currents. As mentioned above, with increasing applied voltage ($V_0 - V > 0.1$ V) the photocurrent saturates to $J_{ph} = qG(E,T)L$. For the 368 nm device, however, the photocurrent intersects the predicted space charge limit and now three regimes appear, as indicated in Figure 10.2b: again, the photocurrent is linear for small applied voltages ($V_0 - V < 0.1$ V).

In the second regime ($0.3\,V < V_0 - V < 0.7$ V), the photocurrent now shows the typical square root dependence of an SCL photocurrent followed by a saturation of the photocurrent ($V_0 - V > 0.7$ V). It is evident that the occurrence of the space charge regime will have a strong effect on the fill factor of the 368 nm device. To further confirm the built-up of space charge in the thick devices, we investigated the dependence of the photocurrent J_{ph} on light intensity I, characterized by $J_{ph} \sim I^{\alpha}$. In Figure 10.6 the coefficient α is given for various effective voltages $V_0 - V$. For the

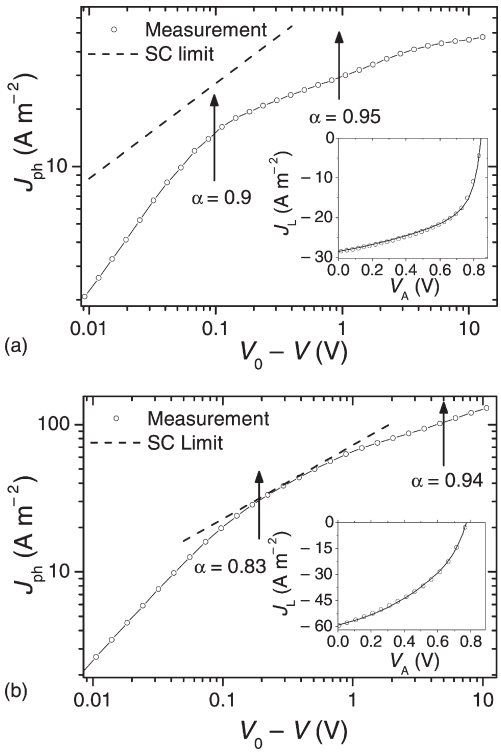

Figure 10.6 Experimental photocurrent density J_{ph} as a function of effective applied voltage $V_0 - V$ under 1 kW m^{-2} illumination for a device consisting of a 128 nm active layer (a) and a 368 nm active layer (b). Circles indicate experimental data, solid line fit of the photocurrent and the dashed line the predicted space charge limit using Equation 10.3. The arrows indicate fits of the intensity dependence $J_{ph} \sim I^{\alpha}$. Inset: current under illumination J_L versus applied voltage V.

thin device α ranges from 0.9 in the linear regime to 0.95 in the saturated regime, indicating that almost no space charge effects occur. For the thick device $\alpha = 0.83$ at $V_0 - V = 0.2$ V, approaching the theoretical value of 3/4 for the pure space-charge-dominated regime [25]. Numerical simulations allow us to disentangle the various loss mechanisms recombination at maximum power point (MPP). First, the average dissociation rate <*P*> decreases for thicker devices as a result of the lower electric field in the device. At the MPP the dissociation efficiency drops from 51.5% for the 128 nm device to 40% for the 368 nm thick solar cell. Furthermore, the recombination losses at MPP increase from 14% for the thin device to 35% for the thick device. This shows that next to space charge formation also the reduced dissociation efficiency and increased recombination losses play a significant role in thick polymer solar cells. The main conclusion for MDMO-PPV:PCBM (1 : 4 wt%) based BHJ solar cells is that an electron mobility of 2×10^{-7} m^2 V^{-1} s^{-1} and a hole mobility of 2×10^{-8} m^2 V^{-1} s^{-1} is sufficient to prevent space charge formation in devices with a thickness of

only 100 nm. However, the mobility difference of a factor of 10 limits the performance of devices of typically 300 nm, a thickness that is required to absorb most of the incoming photons, due to the formation of space charges in combination with an increased recombination. To further improve these thick solar cells, a better hole conductor is needed.

10.3 Annealed P3HT:PCBM-Based Solar Cells

It has been demonstrated by Padinger *et al*. that thermal annealing of devices based on blends of regioregular poly(3-hexylthiophene) (P3HT) and PCBM dramatically improves the external quantum efficiency of these cells [26]. It is well known that an enhanced degree of crystallinity can be induced in polythiophene films by thermal annealing. This controlled crystallization and orientation of polythiophene polymer chains can significantly improve the hole mobility. After annealing, an energy conversion efficiency as high as 3.5% has been reported. Besides this, a red shift of the optical absorption of P3HT inside the blend is observed, providing an improved overlap with the solar emission [27]. To determine the electron and hole mobilities in the P3HT:PCBM blend, we use SCL current–voltage measurements: by using suitable electrodes that either suppress the injection of electrons or holes, hole- or electron-only device are realized, respectively [19]. This technique has been applied to measure either the hole or electron current in blends of P3HT:PCBM as a function of the thermal annealing temperature of the spin-coated films. To fabricate the hole-only devices, palladium was evaporated as a top electrode on an indium tin oxide (ITO)/poly (3,4-ethylenedioxythiophene):poly(4-styrenesulfonate) (PEDOT:PSS)/P3HT:PCBM structure. The work function of PEDOT:PSS matches the highest occupied molecular orbital (HOMO) of P3HT at 4.9 eV, forming an ohmic contact for hole injection [28,29], whereas palladium strongly suppresses electron injection into PCBM due to the large mismatch between its work function and lowest unoccupied molecular orbital (LUMO) of PCBM. To suppress the hole injection into P3HT, the bottom contact must have a low work function. Recently, we have demonstrated that the work function of a noble metal (as silver) can be modified using a self-assembled monolayer (SAM) [30]. This technique works very well and successful electron-only devices were constructed for the P3HT:PCBM blends. Figure 10.7 shows the calculated zero-field mobility of electrons and holes in 50 : 50 wt% blends of P3HT:PCBM devices as a function of the annealing temperature. For comparison, the hole mobility of pristine P3HT, measured under the same experimental conditions, is also shown. It appears from Figure 10.7 that the hole mobility in pristine P3HT is hardly affected by thermal annealing, with a typical value of $(1.4–3.0) \times 10^{-8}\,m^2\,V^{-1}\,s^1$. This mobility was found to be completely field independent and fully consistent with the previously reported values for high molecular weight P3HT (as the one used here) [29]. In contrast, the hole mobility of P3HT in the blend is strongly affected by the

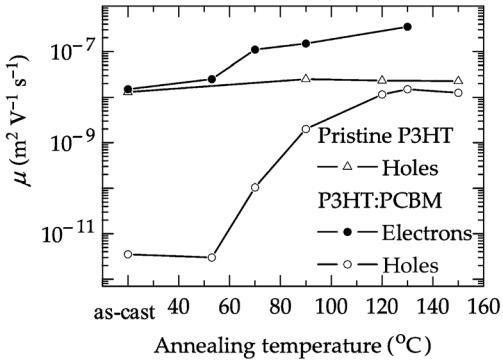

Figure 10.7 Electron and hole mobility in P3HT:PCBM blends as a function of annealing temperature, as well as the hole mobility in pristine P3HT.

presence of PCBM and it drops almost four orders of magnitude for an as-cast device. Upon annealing, however, the mobility starts to increase sharply with an onset at 50–60 °C, followed by saturation to approximately the value of the pristine polymer when the devices are annealed above 120 °C. Moreover, the electron mobility of PCBM in the blend is also affected by thermal annealing: For as-cast films, the electron mobility is $1–2 \times 10^{-8}\,m^2\,V^{-1}\,s^{-1}$, being typically a factor of 5000 higher than the hole mobility. As a result, the charge transport in as-cast films is strongly unbalanced and the current is fully dominated by the electrons.

As a next step, the effect of annealing on the photocurrent of P3HT:PCBM (1 : 1 wt%) solar cells is investigated: Figure 10.8 shows the experimental J_{ph} of P3HT:PCBM blends (50 : 50 wt%) in a double logarithm plot as a function of effective

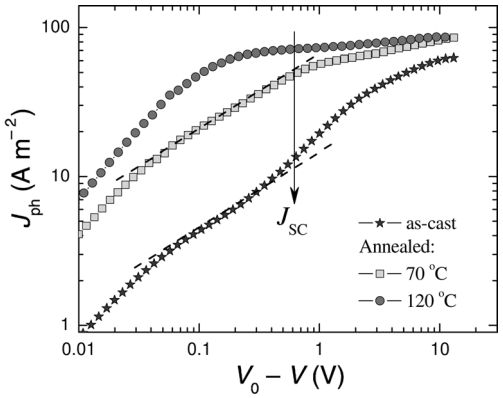

Figure 10.8 Experimental photocurrent (J_{ph}) versus effective applied voltage ($V_0 - V$) of the P3HT:PCBM devices at room temperature, for as-cast device and after thermally annealing of the photoactive layers (see the legend). The device thicknesses (L) are 96 nm and the arrow indicates the position of the short-circuit current (J_{sc}). The dashed lines represent the square root dependence of the J_{ph} on voltage.

applied voltage ($V_0 - V$).The curves correspond to the different postproduction treatment as follows: as-cast thermally annealed at a temperature where the enhancement in hole mobility is maximized (120 °C), and annealed at lower temperature (70 °C). Thermal annealing was performed on complete devices, that is, with the photoactive layer between the electrodes, on the hot plate for a period of 4 min. It appears from Figure 10.8 that the photocurrent shows a strong enhancement after thermal annealing. For the completely annealed device (at 120 °C), the short-circuit current (J_{sc}) increases by a factor of 5, the FF by a factor of 2, and the overall enhancement of the efficiency is about one order of magnitude when compared with the device as-cast. For the device annealed at 70 °C, it is observed that for $V_0 - V < 0.03$ V, the J_{ph} shows linear dependence on voltage, which is caused by the opposite effect of drift and diffusion of charge carriers. Above 0.03 V, however, a square root dependence on voltage of the experimental J_{ph} is observed (dashed line), as is predicted for blends with a large difference in electron and hole mobilities [16]. At even larger voltages, the J_{ph} shows a clear transition to the saturation regime where it becomes limited by the field and temperature dependence of the dissociation of bound electron–hole pairs [20]. These results are distinctly different when the devices are annealed at higher temperature, where the electron and hole transport is more balanced. In that case, no square root dependence of J_{ph} is observed, as seen in the Figure 10.8 by the curve at 120 °C. The occurrence of SCL photocurrents for the devices annealed at only 70 °C has been further confirmed by investigations of the light intensity dependence [31].

These results now allow a true comparison between P3HT:PCBM (1 : 1) and MDMO-PPV:PCBM (1 : 4) blend devices. With respect to the charge transport, the P3HT-based devices have equal mobilities to those measured in MDMO-PPV: PCBM devices. Thus, the increased performance of the P3HT:PCBM solar cells does not originate from an enhanced charge transport, as is often assumed. The main difference, however, is that these identical charge transport properties are realized in blends with different polymer:PCBM weight fractions, namely (1 : 1) versus (1 : 4) for P3HT and MDMO-PPV, respectively. As a result, the larger volume fraction of absorbing material (P3HT), combined with more red-shifted absorption, enlarges the generation rate of charge carriers in 50 : 50 wt% P3HT: PCBM devices by more than a factor of 2, as compared to the 20 : 80 wt% MDMO-PPV:PCBM devices. Combining this with a higher separation efficiency of photogenerated bound electron–hole pairs under short-circuit conditions increases the J_{sc} with more than a factor of 2 for the P3HT-based devices. The most limiting factor of all P3HT-based devices remains, however, the V_{oc}, which is approximately 40% lower as compared to the V_{oc} of the MDMO-based devices. However, the increase in J_{sc} and FF make up for the loss in V_{oc} and, therefore, the power efficiencies of P3HT:PCBM cells are significantly higher. A main conclusion, however, is that also for these annealed P3HT:PCBM solar cells the mobility difference of a factor of 10 will limit the performance of devices with thicknesses exceeding 250 nm. As a result, to further improve the absorption by an increase in the active layer thickness without loss of fill factor also for these devices, the hole mobility needs to be further improved.

10.4
Slowly Dried P3HT:PCBM Solar Cells

Important progress was recently realized by Yang and coworkers, who demonstrated that the efficiency can exceed 4% by controlling the growth rate of the active layer [13]. Slowing down the drying process of the wet films leads to an enhanced self-organization, which is expected to enhance the hole transport in the P3HT. The charge transport properties in these slowly dried P3HT:PCBM blends had been investigated using time-of-flight (TOF) measurements. Electron and hole mobilities of $\mu_e = 7.7 \times 10^{-9}$ and $\mu_h = 5.1 \times 10^{-9}\,m^2\,V^{-1}\,s^{-1}$ were reported, respectively [13]. Remarkably, the reported mobility values for these slowly dried films with superior photovoltaic performance are much lower than the values reported for MDMO-PPV:PCBM and annealed P3HT:PCBM devices: As shown above, for MDMO-PPV:PCBM (1 : 4 wt%) values of $\mu_e = 2.0 \times 10^{-7}$ and $\mu_h = 1.4 \times 10^{-8}\,m^2\,V^{-1}\,s^{-1}$ have been found, and for P3HT:PCBM (1 : 1 wt%) using fast drying and annealing, similar values of $\mu_e = 3.0 \times 10^{-7}$ and $\mu_h = 1.5 \times 10^{-8}\,m^2\,V^{-1}\,s^{-1}$ have been measured. Therefore, the origin of the improved performance after slow drying is not clear. To further investigate the origin of this enhanced performance, we study the hole transport in blends that are spin-coated in chloroform and annealed at 110 °C for 4 min as well as blends that are spin-coated in *ortho*-dichlorobenzene (ODCB) and dried at room temperature in a closed Petri dish. To exclude contributions from the electron transport in the PCBM to the measured current, we used palladium top contacts. In Figure 10.9, the SCL hole-only currents are shown for the fast ($L = 220$ nm) and slowly dried ($L = 408$ nm) films.

For the fast dried and annealed film, the J–V characteristics are quadratic, as expected for an SCL current. The solid line is the calculated current employing a hole

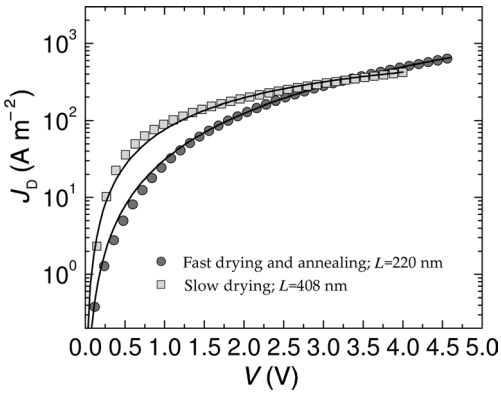

Figure 10.9 Experimental dark current densities (J_D) of the 50 : 50 wt% P3HT:PCBM blend devices, measured at room temperature in the hole-only device configuration. The symbols correspond to different drying conditions of the photoactive layer. The solid lines represent the fit using a model of single carrier SCL current.

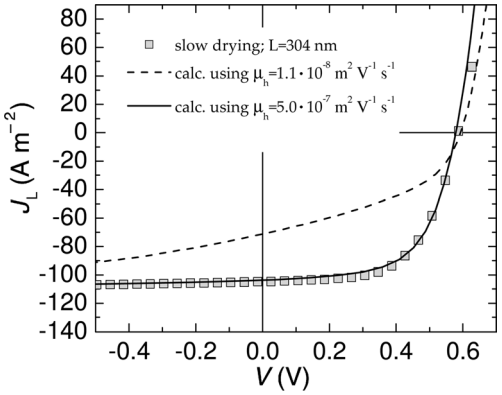

Figure 10.10 Experimental photocurrent (J_L) of a P3HT:PCBM blend solar cell device, prepared by the slow drying method of the photoactive layer (squares), together with the model calculation, using a hole mobility measured in the fast drying film (dashed line) and slow drying film (solid line).

mobility $\mu_h = 1.1 \times 10^{-8}\,m^2\,V^{-1}\,s^{-1}$ similar to the value reported before. For the slowly dried films, a mobility of $\mu_h = 5.0 \times 10^{-7}\,m^2\,V^{-1}\,s^{-1}$ is obtained. Thus, using slow drying, we observe that the hole mobility in the P3HT phase increases by a factor of 45 with respect to the annealed films of Figure 10.9 and compared to a previously reported value for annealed films it is 33 times higher [31]. In Figure 10.10, the photocurrent of the slowly dried device is modeled using the enhanced mobility of $\mu_h = 5.0 \times 10^{-7}\,m^2\,V^{-1}\,s^{-1}$ as input, while the other parameters were kept the same as for the case of the annealed devices: $\mu_e = 3.0 \times 10^{-7}\,m^2\,V^{-1}\,s^{-1}$, $a = 1.8$ nm, and $k_f^{-1} = 7 \times 10^{-5}$ s. Taking the enhanced mobility into account, the calculated photocurrent is in excellent agreement with the measurements. As a reference, the dashed line using the lower mobility of the annealed devices is also included in the plot. As expected, the increase in the mobility leads to a strong enhancement of the FF, going from 42 to 61%. This enhancement of FF together with the increased absorption in the thick film enhances the power efficiency from 3.1 to 3.7%. The role of the increased mobility is that the transition from non-SCL toward the SCL regime is extended to higher thickness. With a mobility of $5.0 \times 10^{-7}\,m^2\,V^{-1}\,s^{-1}$, the 304 nm device is still in the regime where space charge effects do not play a significant role. This is also confirmed by the linear intensity dependence of J_{sc}. As a result, these slowly dried P3HT:PCBM devices are the first plastic solar cells where the electron and hole transport is balanced.

10.5 Conclusions

The enhancement of the hole mobility in MDMO-PPV with two orders of magnitude upon blending with PCBM is the main reason for the achieved 2.5% efficiency in this

type of cells. However, the remaining factor of 10 difference in electron and hole mobility leads to the formation of space charges in thick (>250 nm) devices. The resulting reduction of the fill factor then counteracts the increase in absorption. In annealed P3HT:PCBM solar cells, identical charge transport properties are obtained as compared to the MDMO-PPV:PCBM devices. The increase in performance toward 3.5%, however, results from the fact that these mobilities are obtained in a blend of 1 : 1 wt%, as compared to the 1 : 4 wt% for the MDMO-PPV:PCBM case. The larger polymer fraction in the blend, together with a red shift of the absorption, leads to an increase in the amount of absorbed light resulting in a higher efficiency. For slowly dried P3HT:PCBM devices, a balanced charge transport is obtained. As a result, for thick devices no significant space charge formation and reduction of the fill factor occur. The increased absorption then enhances the efficiency to typically 4%.

Acknowledgments

The authors especially acknowledge the contributions of Kees Hummelen, Bert de Boer, Jur Wildeman, Minte Mulder, Alex Sieval, and Edsger Smits to this work. These investigations were financially supported by the Dutch Ministries of EZ, O&W, and VROM through the EET program (EETK97115). The work of L. J. A. Koster forms part of the research program of the Dutch Polymer Institute (#323).

References

1 Green, M.A., Emery, K., King, D.L., Hishikawa, Y. and Warta, W. (2006) *Progress in Photovoltaics*, **14**, 455.

2 Kallmann, H. and Pope, M. (1959) *Journal of Chemical Physics*, **30**, 585.

3 Gomes da Costa, P. and Conwell, E.M. (1993) *Physical Review B: Condensed Matter*, **48**, 1993.

4 Marks, R.N., Halls, J.J.M., Bradley, D.D.C., Friend, R.H. and Holmes, A.B. (1994) *Journal of Physics of Condensed Matter*, **6**, 1379.

5 Barth, S. and Bässler, H. (1997) *Physical Review Letters*, **79**, 4445.

6 Tang, C.W. (1986) *Applied Physics Letters*, **48**, 183.

7 Sariciftci, N.S., Smilowitz, L., Heeger, A.J. and Wudl, F. (1992) *Science*, **258**, 1474.

8 Halls, J.J.M., Pichler, K., Friend, R.H., Moratti, S.C. and Holmes, A.B. (1996) *Applied Physics Letters*, **68**, 3120.

9 Markov, D.E., Tanase, C., Blom, P.W.M. and Wildeman, J. (2005) *Physical Review B: Condensed Matter*, **72**, 045217.

10 Markov, D.E., Amsterdam, E., Blom, P.W.M., Sieval, A.B. and Hummelen, J.C. (2005) *Journal of Physical Chemistry A*, **109**, 5266.

11 Yu, G., Gao, J., Hummelen, J.C., Wudl, F. and Heeger, A.J. (1995) *Science*, **270**, 1789.

12 Shaheen, S.E., Brabec, C.J., Sariciftci, N.S., Padinger, F., Fromherz, T. and Hummelen, J.C. (2001) *Applied Physics Letters*, **78**, 841.

13 Li, G., Shrotriya, V., Huang, J., Yao, Y., Moriarty, T., Emery, K. and Yang, Y. (2005) *Nature Materials*, **4**, 864.

14 Goodman, A.M. and Rose, A. (1971) *Journal of Applied Physics*, **42**, 2823.

15 Sokel, R. and Hughes, R.C. (1982) *Journal of Applied Physics*, **53**, 7414.

16 Mihailetchi, V.D., Wildeman, J. and Blom, P.W.M. (2005) *Physical Review Letters*, **94**, 126602.

17 Blom, P.W.M., de Jong, M.J.M. and Vleggaar, J.J.M. (1996) *Applied Physics Letters*, **68**, 3308.

18 Mihailetchi, V.D., van Duren, J.K.J., Blom, P.W.M., Hummelen, J.C., Janssen, R.A.J., Kroon, J.M., Rispens, M.T., Verhees, W.J.H. and Wienk, M.M. (2003) *Advanced Functional Materials*, **13**, 43.

19 Melzer, C., Koop, E., Mihailetchi, V.D. and Blom, P.W.M. (2003) *Advanced Functional Materials*, **14**, 865.

20 Mihailetchi, V.D., Koster, L.J.A., Hummelen, J.C. and Blom, P.W.M. (2004) *Physical Review Letters*, **93**, 216601.

21 Braun, C.L. (1984) *Journal of Chemical Physics*, **80**, 4157.

22 Koster, L.J.A., Smits, E.C.P., Mihailetchi, V.D. and Blom, P.W.M. (2005) *Physical Review B: Condensed Matter*, **72**, 085205.

23 Schilinsky, P., Waldauf, C., Hauch, J. and Brabec, C.J. (2004) *Journal of Applied Physics*, **95**, 2816.

24 Riedel, I. and Dyakonov, V. (2004) *Physica Status Solidi a: Applied Research*, **201**, 1332.

25 Lenes, M., Koster, L.J.A., Mihailetchi, V.D. and Blom, P.W.M. (2006) *Applied Physics Letters*, **88**, 243502.

26 Padinger, F., Rittberger, R.S. and Sariciftci, N.S. (2003) *Advanced Functional Materials*, **13**, 85.

27 Chirvase, D., Parisi, J., Hummelen, J.C. and Dyakonov, V. (2004) *Nanotechnology*, **15**, 1317.

28 Kim, Y., Choulis, S.A., Nelson, J., Bradley, D.D.C., Cook, S. and Durrant, J.R. (2005) *Applied Physics Letters*, **86**, 063502.

29 Goh, C., Kline, R.J., McGehee, M.D., Kadnikova, E.N. and Fréchet, J.M.J. (2005) *Applied Physics Letters*, **86**, 122110.

30 de Boer, B., Hadipour, A., Mandoc, M.M., van Woudenbergh, T. and Blom, P.W.M. (2005) *Advanced Materials*, **17**, 621.

31 Mihailetchi, V.D., Xie, H., de Boer, B., Koster, L.J.A. and Blom, P.W.M. (2006) *Advanced Functional Materials*, **16**, 599.